

Light propagation from fluorescent probes in biological tissues by coupled time-dependent parabolic simplified spherical harmonics equations

Jorge Bouza Domínguez^{1,*} and Yves Bérubé-Lauzière^{1,2}

¹Laboratoire TomOptUS, Département de génie électrique et de génie informatique,
Faculté de génie, Université de Sherbrooke,
2500 boul. Université, Sherbrooke, Québec, J1K 2R1, Canada

²Centre d'imagerie moléculaire de Sherbrooke (CIMS) - Centre de recherche clinique Étienne-Le Bel du CHUS,
3001, 12e Avenue Nord, Sherbrooke, Québec, J1H 5N4, Canada

*jorgbd@gmail.com

Abstract: We introduce a system of coupled time-dependent parabolic simplified spherical harmonic equations to model the propagation of both excitation and fluorescence light in biological tissues. We resort to a finite element approach to obtain the time-dependent profile of the excitation and the fluorescence light fields in the medium. We present results for cases involving two geometries in three-dimensions: a homogeneous cylinder with an embedded fluorescent inclusion and a realistically-shaped rodent with an embedded inclusion alike an organ filled with a fluorescent probe. For the cylindrical geometry, we show the differences in the time-dependent fluorescence response for a point-like, a spherical, and a spherically Gaussian distributed fluorescent inclusion. From our results, we conclude that the model is able to describe the time-dependent excitation and fluorescent light transfer in small geometries with high absorption coefficients and in nondiffusive domains, as may be found in small animal diffuse optical tomography (DOT) and fluorescence DOT imaging.

© 2011 Optical Society of America

OCIS codes: (170.3660) Light propagation in tissues; (170.6280) Spectroscopy, fluorescence and luminescence; (170.6920) Time-resolved imaging.

References and links

1. R. Weissleder and V. Ntziachristos, "Shedding light onto live molecular targets," *Nat. Med.* **9**(1), 123–128 (2003).
2. A. H. Hielscher, "Optical tomography imaging of small animals," *Curr. Opin. Biotechnol.* **16**(1), 79–88 (2005).
3. V. Ntziachristos, "Fluorescence molecular imaging," *Annu. Rev. Biomed. Eng.* **8**(1), 1–33 (2006).
4. J. Rao, A. Dragulescu-Andrasi, and H. Yao, "Fluorescence imaging in vivo: recent advances," *Curr. Opin. Biotechnol.* **18**(1), 17–25 (2007).
5. A. D. Klöse, "Radiative transfer of luminescence light in biological tissue," in *Light Scattering Reviews 4 Single Light Scattering and Radiative Transfer*, A. A. Kokhanovsky, ed., (Springer, 2009), pp 293–345.
6. R. E. Nothdurft, S. V. Patwardhan, W. Akers, Y. Ye, S. Achilefu, and J. P. Culver, "In vivo fluorescence lifetime tomography," *J. Biomed. Opt.* **14**(2), 024004 (2009).
7. J. Klohs, J. Steinbrink, R. Bourayou, S. Mueller, R. Cordell, K. Licha, M. Schirner, U. Dirnagl, U. Lindauer, and A. Wunder, "Near-infrared fluorescence imaging with fluorescently labeled albumin: a novel method for non-invasive optical imaging of blood-brain barrier impairment after focal cerebral ischemia in mice," *J. Neurosci. Methods* **180**(1), 126–132 (2009).
8. S. Mordon, J. M. Devoisselle, and V. Maunoury, "In vivo pH measurement and imaging of tumor tissue using a pH-sensitive fluorescent probe (5,6-carboxyfluorescein): instrumental and experimental studies," *Photochem. Photobiol.* **60**(3), 274–279 (1994).
9. R. Weissleder and U. Mahmood, "Molecular imaging," *Radiology* **219**(2), 316–333 (2001).
10. E. M. C. Hillman and A. Moore, "All-optical anatomical co-registration for molecular imaging of small animals using dynamic contrast," *Nat. Photonics* **1**(9), 526–530 (2007).

11. M. L. Landsman, G. Kwant, G. A. Mook, and W. G. Zijlstra, "Light-absorbing properties, stability, and spectral stabilization of indocyanine green," *J. Appl. Physiol.* **40**(4), 575–583 (1976).
12. X. Li, B. Beauvoit, R. White, Sh. Nioka, B. Chance, and A. G. Yodh, "Tumor localization using fluorescence of indocyanine green (ICG) in rat models," *Proc. SPIE* **2389**, 789–797 (1995).
13. Ch. Haritoglou, A. Gandorfer, M. Schaumberger, R. Tadayoni, A. Gandorfer, and A. Kampik, "Light-absorbing properties and osmolarity of indocyanine-green depending on concentration and solvent medium," *Invest. Ophthalmol. Vis. Sci.* **44**(6), 2722–2729 (2003).
14. A. B. Milstein, S. Oh, K. J. Webb, C. A. Bouman, Q. Zhang, D. A. Boas, and R. P. Millane, "Fluorescence optical diffusion tomography," *Appl. Opt.* **42**(16), 3081–3094 (2003).
15. X. Intes, J. Ripoll, Y. Chen, Sh. Nioka, A. G. Yodh, and B. Chance, "In vivo continuous-wave optical breast imaging enhanced with Indocyanine Green," *Med. Phys.* **30**(6), 1039–1047 (2003).
16. L. Wang and H. Wu, in *Biomedical Optics: Principles and Imaging* (Wiley-Interscience, 2007).
17. S. R. Arridge, "Optical tomography in medical imaging," *Inverse Probl.* **15**(2), R41–R93 (1999).
18. A. Klose and E. Larsen, "Light transport in biological tissue based on the simplified spherical harmonics equations," *J. Comput. Phys.* **220**(1), 441–470 (2006).
19. T. Tarvainen, *Computational Methods for Light Transport in Optical Tomography*, PhD Thesis, University of Kuopio, (2006).
20. L. Martí-López, J. Bouza-Domínguez, and J. C. Hebden, "Interpretation of the failure of the time-independent diffusion equation near a point source," *Opt. Commun.* **242**(1-3), 23–43 (2004).
21. A. H. Hielscher, R. E. Alcouffe, and R. L. Barbour, "Comparison of finite-difference transport and diffusion calculations for photon migration in homogeneous and heterogeneous tissues," *Phys. Med. Biol.* **43**(5), 1285–1302 (1998).
22. V. Ntziachristos and B. Chance, "Accuracy limits in the determination of absolute optical properties using time-resolved NIR spectroscopy," *Med. Phys.* **28**(6), 1115–1124 (2001).
23. D. C. Comsa, T. J. Farrell, and M. S. Patterson, "Quantitative fluorescence imaging of point-like sources in small animals," *Phys. Med. Biol.* **53**(20), 5797–5814 (2008).
24. J. Pichette, E. Lapointe, and Y. Bérubé-Lauzière, "Time-domain 3D localization of fluorescent inclusions in a thick scattering medium," *Proc. SPIE* **7099**, 709907, 709907-12 (2008).
25. J. Pichette, E. Lapointe, and Y. Bérubé-Lauzière, "Three-dimensional localization of discrete fluorescent inclusions from multiple tomographic projections in the time-domain," *Proc. SPIE* **7174**, 71741A, 71741A-10 (2009).
26. E. W. Larsen, J. E. Morel, and J. M. McGhee, "Asymptotic derivation of the multigroup P_1 and simplified P_N equations with anisotropic scattering," *Nucl. Sci. Eng.* **123**, 328 (1996).
27. D. I. Tomasevic and E. W. Larsen, "The simplified P_2 approximation," *Nucl. Sci. Eng.* **122**, 309–325 (1996).
28. P. S. Brantley and E. W. Larsen, "The simplified P_3 approximation," *Nucl. Sci. Eng.* **134**, 121 (2000).
29. M. Frank, A. Klar, E. W. Larsen, and S. Yasuda, "Approximate models of radiative transfer," *Bull. Inst. Math. Acad. Sin.* **2**, 409–432 (2007).
30. P. Kotiluoto, J. Pyry, and H. Helminen, "Multitrans SP_3 code in coupled photon-electron transport problems," *Radiat. Phys. Chem.* **76**(1), 9–14 (2007).
31. M. Frank, A. Klar, E. Larsen, and S. Yasuda, "Time-dependent simplified P_N approximation to the equations of radiative transfer," *J. Comput. Phys.* **226**(2), 2289–2305 (2007).
32. M. Chu, K. Vishwanath, A. D. Klose, and H. Dehghani, "Light transport in biological tissue using three-dimensional frequency-domain simplified spherical harmonics equations," *Phys. Med. Biol.* **54**(8), 2493–2509 (2009).
33. Y. Bérubé-Lauzière, V. Issa, and J. B. Domínguez, "Simplified spherical harmonics approximation of the time-dependent equation of radiative transfer for the forward problem in time-domain diffuse optical tomography," *Proc. SPIE* **7174**, 717403, 717403-11 (2009).
34. J. B. Domínguez and Y. Bérubé-Lauzière, "Diffuse light propagation in biological media by a time-domain parabolic simplified spherical harmonics approximation with ray-divergence effects," *Appl. Opt.* **49**(8), 1414–1429 (2010).
35. F. Gao, H. Zhao, and Y. Yamada, "Improvement of image quality in diffuse optical tomography by use of full time-resolved data," *Appl. Opt.* **41**(4), 778–791 (2002).
36. E. Hillman, *Experimental and theoretical investigations of near infrared tomographic imaging methods and clinical applications*, Ph.D. Thesis, University College London, (2002).
37. D. Hyde, *Improving Forward Matrix Generation and Utilization for Time Domain Diffuse Optical Tomography*, MSc Thesis, Dept. Elect. Comp. Eng., Northeastern University, (2004)
38. H. Zhao, F. Gao, Y. Tanikawa, and Y. Yamada, "Time-resolved diffuse optical tomography and its application to in vitro and in vivo imaging," *J. Biomed. Opt.* **12**(6), 062107 (2007).
39. J. Mobley and T. Vo-Dinh, "Optical properties of tissue," in *Biomedical Photonics Handbook*, T. Vo-Dinh ed. (CRC Press, 2003), pp. 20–95.
40. T. Svensson, S. Andersson-Engels, M. Einarsdóttir, and K. Svanberg, "In vivo optical characterization of human prostate tissue using near-infrared time-resolved spectroscopy," *J. Biomed. Opt.* **12**(1), 014022 (2007).
41. M. Born and E. Wolf, *Principles of Optics*, 7th ed. (Cambridge U. Press, 2003).
42. S. R. Arridge, "Photon-measurement density functions. Part I: Analytical forms," *Appl. Opt.* **34**(31), 7395–7409 (1995).

43. L. V. Wang and S. L. Jacques, "Sources of error in calculation of optical diffuse reflectance from turbid media using diffusion theory," *Comput. Meth. Prog. Bio.* **61**(3), 163–170 (2000).
44. A. Ishimaru, *Wave Propagation and Scattering in Random Media*, (Academic Press, 1978).
45. G. Eason, A. R. Veitch, R. M. Nisbet, and F. W. Turnbull, "The theory of back-scattering of light by blood," *J. Phys. D Appl. Phys.* **11**(10), 1463–1479 (1978).
46. A. H. Hielscher, R. E. Alcouffe, and R. L. Barbour, "Comparison of finite-difference transport and diffusion calculations for photon migration in homogeneous and heterogeneous tissues," *Phys. Med. Biol.* **43**(5), 1285–1302 (1998).
47. W. Cheong, S. Prah, and A. Welch, "A review of the optical properties of biological tissues," *IEEE J. Quantum Electron.* **26**(12), 2166–2185 (1990).
48. M. Schweiger, S. R. Arridge, and D. T. Delpy, "Application of the finite-element method for the forward and inverse models in optical tomography," *J. Math. Imaging Vis.* **3**(3), 263–283 (1993).
49. S. R. Arridge, M. Schweiger, M. Hiraoka, and D. T. Delpy, "A finite element approach for modeling photon transport in tissue," *Med. Phys.* **20**(2), 299–309 (1993).
50. G. Abdoulaev and A. Hielscher, "Three-dimensional optical tomography with the equation of radiative transfer," *J. Electron. Imaging* **12**(4), 594–601 (2003).
51. L. Hervé, A. Koenig, A. Da Silva, M. Berger, J. Boutet, J. M. Dinten, P. Peltié, and P. Rizo, "Noncontact fluorescence diffuse optical tomography of heterogeneous media," *Appl. Opt.* **46**(22), 4896–4906 (2007).
52. T. Tarvainen, M. Vauhkonen, V. Kolehmainen, J. P. Kaipio, and S. R. Arridge, "Utilizing the radiative transfer equation in optical tomography," *PIERS Proceedings* **4**, 730–735 (2008).
53. M. Schweiger, S. R. Arridge, M. Hiraoka, and D. T. Delpy, "The finite element method for the propagation of light in scattering media: boundary and source conditions," *Med. Phys.* **22**(11), 1779–1792 (1995).
54. S. Prah, "Optical absorption of Indocyanine Green," <http://omlc.ogi.edu/spectra/icg/index.html>.
55. K. D. Paulsen and H. Jiang, "Spatially varying optical property reconstruction using a finite element diffusion equation approximation," *Med. Phys.* **22**(6), 691–701 (1995).
56. D. J. Durian and J. Rudnick, "Spatially resolved backscattering: implementation of extrapolation boundary condition and exponential source," *J. Opt. Soc. Am. A* **16**(4), 837–844 (1999).
57. G. Paumgartner, P. Probst, R. Kraines, and C. M. Leevy, "Kinetics of indocyanine green removal from the blood," *Ann. N. Y. Acad. Sci.* **170**(1 The Hepatic C), 134–147 (1970).
58. P. Gallant, A. Belenkov, G. Ma, F. Lesage, Y. Wang, D. Hall, and L. McIntosh, "A quantitative time-domain optical imager for small animals *in vivo* fluorescence studies" in *Biomedical Topical Meeting*, OSA Technical Digest (Optical Society of America, 2004), paper WD2.
59. B. Dogdas, D. Stout, A. F. Chatziioannou, and R. M. Leahy, "Digimouse: a 3D whole body mouse atlas from CT and cryosection data," *Phys. Med. Biol.* **52**(3), 577–587 (2007).
60. R. Klette, K. Schlüns, and A. Koschan, *Computer Vision – Three-Dimensional Data from Images*, (Springer, 1998).
61. M. Comtois and Y. Bérubé-Lauzière, "Optical surface metrology in 3D for small animal non-contact diffuse optical tomography," *Proc. SPIE* **6796**, 679605, 679605-9 (2007).
62. <http://www.art.ca/en/preclinical/optix-mx3/acquisition-system.php>, Web page consulted on 15 Dec. 2010.

1 Introduction

Fluorescence biomedical imaging techniques offer the possibility to differentiate diseased from normal tissues, pursue the progression of a disease *in vivo* at a molecular level and monitor possible treatments via fluorescent probes [1–6]. The main methods in fluorescent imaging can be classified as direct or indirect [5]. Direct methods make use of active probes, *i.e.* fluorophores attached to affinity ligands which are target-specific [1] and activatable probes *i.e.* molecules which are carriers of quenched fluorophores that are freed in the presence of specific enzymes [4,5]. Indirect methods are used for studying gene expression and gene regulation and involve the introduction of transgenes. Transgenes are responsible for the production of fluorescent proteins which in turn act as probes [4].

At a macroscopic level, imaging fluorescent probes is often carried on whole-body small animals. The extension to *in vivo* small animal studies, known as *in vivo* fluorescence imaging, allows visualizing functional processes, *e.g.* in the brain [7], during physiological states [8] as well as visualizing complex biological processes at the molecular level, leading to so-called molecular imaging [9]. Exploiting fluorescence *in vivo* dynamics also allows segmenting organs in images [10]. This modality enables pharmacokinetic studies and evaluation of dynamic experimental animal models. In addition, non-specific exogenous fluorescent dyes like Indocyanine Green (ICG) are used in studies of demarcation of neoplastic tissue providing information about angiogenesis, and in particular the permeability of the ensuing vascularization [11–15].

Fluorescence optical imaging deep into tissues of small animals (depths > 1 cm) is possible owing to the availability of dyes and photodynamic agents that emit in the near-infrared (NIR) wavelength regime from about 650nm to 1000nm, so-called the therapeutic window as light is less absorbed in that region. At NIR wavelengths, excitation and fluorescence light can travel significant distances in biological tissues. Propagation of light in biological tissues is commonly described by standard radiative transfer theory (RTT) [16], since tissues both absorb and scatter light. In RTT, it is assumed that light undergoes a series of absorption and scattering events while propagating, combined with reflection and refraction at boundaries between media with different refractive indices [16]. The propagation of light in the medium is then mathematically described by equations and associated boundary conditions to account for reflection and refraction. Such equations, referred to as the *forward model*, can be used to determine the light field profile within the medium. The task of assessing the light distribution in the medium using the equations of the forward model when *a priori* knowledge of the geometry, the optical properties of the medium, and the distribution of sources, is known as the *forward problem* [5,17].

Among the forward models used for describing light propagation in biological tissues, we have stochastic approaches based on Monte Carlo simulations that resort to microscopic modeling of how light interacts with a medium, and deterministic approaches based on field quantities obeying partial differential equations (PDEs) or integro-PDEs. For the latter, we have the standard radiative transfer equation (RTE), and approximations thereof such as the P_N equations and the diffusion equation (DE) [16,17]. The RTE is considered as the most accurate deterministic model of light propagation in RTT [16], but its numerical implementation is computationally intensive [18]. For the P_N equations (which are in fact a hierarchy of approximations of different orders), although they are approximations to the RTE, they are also computationally demanding when solved numerically [19]. Among all equations, the DE is the easiest to solve, and it is capable of describing light propagation in highly scattering media. However, the DE fails in small geometries, in regions with high absorption or low scattering (*e.g.* voids such as lungs), and near sources [20,21]. Moreover, in the time domain, the DE does not reproduce early time experimental data, partly because of the few scattering events the photons undergo [22].

The drawbacks of the DE make its use to describe light propagation in biological tissues questionable when the aforementioned situations occur. In practice, the values of the absorption coefficient in the NIR spectrum are often comparable with the values of the scattering coefficient, in which case the DE is not valid. This happens when dealing with highly vascularized tissues (*e.g.* heart, liver, *etc.*, see reported values in [23]). Another circumstance comes about in optical imaging of NIR-activable fluorescent probes, which requires calculating the profile of the optical field in the tissue at the excitation wavelength. Practical values of the concentration of the fluorophore may lead to high absorption levels of the excitation light [11,12,14,24,25] which makes the DE inappropriate as a forward model.

To overcome the disadvantages of the current forward models, the simplified spherical harmonics approximation to the RTE (SP_N) used in nuclear reactor theory to study neutron transport [26–28], was brought to biomedical optics for the time-independent case [18]. The SP_N approximation transforms the time-independent RTE into a set of coupled diffusion-like PDEs (SP_N equations) involving moments of the radiance function. In general, the SP_N method avoids the complexities of the P_N approximation which involves mixed spatial derivatives. The use of the SP_N equations for modeling light propagation was shown by Klose and Larsen to significantly reduce the computational burden compared with the RTE in the time-independent case, while providing near to RTE accuracy [18]. SP_N methods have arisen in the literature covering continuous wave (CW), frequency-domain, and time-domain (TD) regimes [18,26–34]. TD methods involve the calculation of time-point-spread-functions (TPSFs) which carry more information about tissue optical properties than measurements based on frequency-domain or CW methods [16,35–38]. In addition, TD methods allow direct

access to the fluorescence lifetime, which conveys information about local metabolite concentrations or environmental conditions within tissues (see [1–6] and references therein).

In a previous paper [34], we derived TD parabolic SP_N equations (the TD-p SP_N model) and compared them with the DE and Monte Carlo simulations. The results obtained support the TD-p SP_N model as a suitable approximation to the RTE for problems in biomedical optics where radiative transfer theory is employed. Particularly, the TD-p SP_N model gives better results than the DE in near non-diffusive media and for small inhomogeneities with high absorption coefficients. Additionally, the TD-p SP_N model better reproduces the rising edge of the time-dependent fluence rate obtained with Monte Carlo simulations than the DE. Also, the TD-p SP_N model can accurately describe the propagation of light near sources in regions where the DE fails. Considering the advantages of the TD-p SP_N model, it will thus be useful to proceed with its extension for studying the time-dependent fluorescent response of a fluorescent agent distributed in biological tissues. The subject of this paper is the modeling of the time-dependent response of fluorescent agents in biological tissues and the ensuing time-domain propagation of light therein. Towards this end, we herein develop, for the first time, a set of equations (a model) along with a complete numerical scheme for modeling the propagation of excitation and fluorescence light in the *time domain* in complex 3D geometries based on the simplified spherical harmonics approximation (SP_N). Our objective is to be able to compute efficiently (*i.e.* reduce computation time) and accurately (*i.e.* near to RTE) both the time and spatial dependencies of the excitation and fluorescence light fields inside an absorbing and scattering medium with complex geometry using the SP_N method coupled with the finite element method. This will be demonstrated through numerical results for complex geometries with exogenous fluorescent probes (our approach also naturally applies to other types of fluorescence sources, such as fluorescent proteins, or endogenous fluorophores). We next outline the contents of the paper.

2 Outline of the paper

In this work we make a natural extension of the TD-p SP_N model to address the forward problem of describing the time-dependent light field spatial distribution emitted by a fluorescent agent distributed inside a biological tissue. As a result, we obtain two coupled sets of parabolic PDEs of the TD-p SP_N type and associated boundary conditions with matrix coefficients. Forward problems at both excitation and fluorescent wavelengths are therefore conceptually reduced to calculating light propagation from internal sources using TD-p SP_N equations, an approach validated in a previous study [34]. To achieve this we resort to a finite element method (FEM) approach for representing the spatial dependence of the system of equations. Then, we build a numerical scheme by which we can compute the time-dependent profile of the excitation and of the fluorescence fluence rates for inhomogeneous media with arbitrary geometries, such as biological tissues.

We perform numerical experiments for two different geometries and study the fluorescence response in the time domain. The first geometry is a small cylinder with a 3 cm height and 1.5 cm radius having tissue-like optical properties, and resembling a small volume of biological tissue. For this geometry we assess the effects of embedding three types of fluorescent inclusions with optical properties mimicking those of an ICG solution: a point-like, a spherical and a spherically symmetric fluorescent inclusion having a radially Gaussian distributed absorption. With those physical situations we take into account practical cases occurring in small animal fluorescence diffuse optical tomography (FDOT). We note, by generating TD data, that point and non-point fluorescent inclusions cause different temporal profiles of the fluorescence response, a feature that can be studied in depth with our model.

The second geometry is a three-dimensional realistically-shaped animal model resembling a rat or a mouse with an embedded fluorescent inclusion similar to an organ. The set of optical properties used in the second numerical experiment is identical to the first experiment. However, the physical situation concerning the geometry and the distribution of the excitation

sources is more complex. The experiments aim to reproduce practical cases of *in vivo* fluorescence imaging with increasing complexity in the calculation of the excitation and fluorescent radiative fields. For both geometries considered, the effects of the high absorption coefficient of the fluorescent inclusion are observed for different times. The fluorescence light transfer from an extended source and the expected decay of the fluorescence field with time are modeled. Finally, since our model inherits the features of the TD-pSP_N equations, it is worthwhile to stress on its advantages, which are also presented in the performed numerical experiments. As will be seen, the model accurately describes the excitation and fluorescence light transfer in small geometries containing vascularized tissues (high absorption coefficient values $\sim 1\text{cm}^{-1}$ [39]). In addition, that property is extended to fluorescent probe distributions with high absorption coefficient. What's more, the anisotropy of the radiative field near the injection of excitation light, such as coming from laser beams, is taken into account. In addition, ray divergence effects owing to the presence of internal sources are considered in the model.

3 Fluorescence light transfer in biological tissue

To study the fluorescence light transfer in biological tissues, we consider the time-dependent excitation of fluorophores with ultra-short laser pulses at the so-called excitation wavelength λ^x and their transient response over time at a given wavelength λ^m of the emission spectrum. Such phenomena can be modeled by time-dependent coupled radiative transfer equations [5]. We first carry on by describing the time-dependent excitation light transfer through the TD-pSP_N model. Then we will discuss how this couples with the time dependent fluorescence light transfer, also described by a TD-pSP_N model.

3.1 Time-dependent excitation light transfer

Let us assume that a volume of biological tissue V , delimited by a boundary ∂V , is illuminated by a discrete distribution of external sources at a wavelength λ^x , see Fig. 1. Then, we can use the RTE with source divergence (RTE_{SD}) to describe the propagation of the excitation light [34].

$$\left[\frac{\eta^x}{c} \frac{\partial}{\partial t} + \hat{\mathbf{s}} \cdot \nabla + \mu_t^x(\mathbf{r}) + \mu_a^{x \rightarrow m}(\mathbf{r}) \right] L^x(\mathbf{r}, \hat{\mathbf{s}}, t) = \mu_s^x(\mathbf{r}) \int_{4\pi} p^x(\mathbf{r}, \hat{\mathbf{s}}, \hat{\mathbf{s}}') L^x(\mathbf{r}, \hat{\mathbf{s}}', t) d\Omega', \quad (1)$$

where $L^x(\mathbf{r}, \hat{\mathbf{s}}, t)$ is the radiance at a point \mathbf{r} in the direction specified by the unit vector $\hat{\mathbf{s}}$, η^x is the refractive index at the excitation wavelength λ^x , c is the speed of light in vacuum, $\mu_t^x = \mu_a^x + \mu_s^x$ and μ_s^x are the position-dependent transport and scattering coefficients of the medium (μ_a^x is the absorption coefficient of the medium), respectively; $\mu_a^{x \rightarrow m}$ is the absorption coefficient of the fluorescent distribution at wavelength λ^x , $p^x(\mathbf{r}, \hat{\mathbf{s}}, \hat{\mathbf{s}}')$ is the normalized scattering phase function at that wavelength and $d\Omega'$ is a differential element of solid angle.

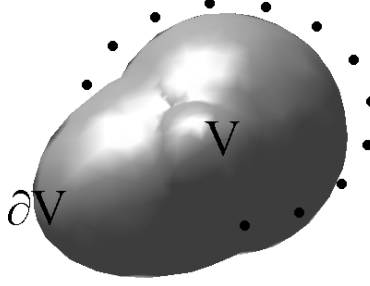


Fig. 1. Volume of biological tissue. Black dots represent a distribution of discrete light sources illuminating the volume.

The symbol ∇ denotes the gradient operator with respect to the coordinates of the position vector \mathbf{r} . Eq. (1) is identical to the standard RTE because, for the time being, only external sources are considered, and in the absence of internal sources ray divergence effects do not need to be considered [34]. We nevertheless prefer to pose the RTE_{SD} as the forward model instead of the RTE, in order to account for the presence of excitation sources embedded in the tissue, as in the case, for example, of optical imaging of the prostate [40]. In such situations, ray divergence effects should be included in Eq. (1) by considering associated source terms and adding the consequent divergence coefficient (see [34] for details on how to proceed).

The corresponding boundary conditions for Eq. (1) are

$$L^x(\mathbf{r}, \hat{\mathbf{s}}, t) = B_r^x(\mathbf{r}, \hat{\mathbf{s}})\delta(t) + R_F^x(\hat{\mathbf{s}}' \cdot \hat{\mathbf{n}})L^x(\mathbf{r}, \hat{\mathbf{s}}', t), \quad \mathbf{r} \in \partial V, \quad \hat{\mathbf{s}}' = \hat{\mathbf{s}} - 2(\hat{\mathbf{s}} \cdot \hat{\mathbf{n}}), \quad \hat{\mathbf{s}} \cdot \hat{\mathbf{n}} < 0, \quad (2)$$

where $B_r^x(\mathbf{r}, \hat{\mathbf{s}})$ is the *transmitted* radiance of the distribution of external sources, $\delta(t)$ represents the Dirac delta function in time, $\hat{\mathbf{n}}$ is the outward pointing unit normal to the boundary ∂V and $R_F^x(\hat{\mathbf{s}} \cdot \hat{\mathbf{n}})$ is the angle-dependent Fresnel reflection coefficient at λ^x [41].

The type of measurements related to the forward model posed by Eqs. (1) and (2) depends on the experimental conditions and can take on different forms [17,42]. It is common to use the normal component of the exiting photon current density vector (or outward power flux) J_n^x (at the excitation wavelength λ^x) [5,18]

$$J_n^x = \int_{\hat{\mathbf{s}} \cdot \hat{\mathbf{n}} > 0} \left[1 - R_F^x(\hat{\mathbf{s}} \cdot \hat{\mathbf{n}}) \right] \hat{\mathbf{s}} \cdot \hat{\mathbf{n}} L^x(\mathbf{r}, \hat{\mathbf{s}}, t) d\Omega, \quad (3)$$

or an average thereof over a spot, which usually has a typical dimension on the order of one to a few millimeters.

3.1.1 TD- pSP_N equations for excitation light transfer

In biomedical optics it is very common to use collimated laser beams as external sources of excitation. The photon flux is highly anisotropic inside the medium near the point on the surface where the light from the source impinges the medium. Basically, the fluence profile near that point resembles a needle-like shape. Here, source modeling becomes an important aspect of the calculations. Neglecting the radiative field's anisotropy due to the incident source or otherwise, converting a laser beam into an isotropic point source, generates the most significant error in calculations near sources [16,43]. Hence, the use of low-order transport approximations to Eq. (1) in this region is poorly justified when compared with predictions of RTE calculations (see [44,45] for considerations about the source term). If regions with optical properties that defy the diffusion regime *i.e.* $\mu_a/\mu_s' \geq 0.1$ [46] are close to this zone, results deteriorate even more since the field becomes more anisotropic (light is less diffused).

Such situations may arise in small animal imaging where regions with high absorption coefficients such as vascularized tissues (*e.g.* superficial vasculature, skin tumors, *etc.*) are present inside the medium and near impingement points of external sources. A better alternative is to divide the radiance into the reduced $L_r^x(\mathbf{r}, \hat{\mathbf{s}}, t)$ and the diffuse $L_d^x(\mathbf{r}, \hat{\mathbf{s}}, t)$ components [44] and apply the low-order transport approximation to the diffuse component $L_d^x(\mathbf{r}, \hat{\mathbf{s}}, t)$. The reduced component $L_r^x(\mathbf{r}, \hat{\mathbf{s}}, t)$ is that part of the photon flux that decreases along a direction $\hat{\mathbf{s}}$ due to scattering and absorption and which originates from the source distribution, whereas the diffuse component $L_d^x(\mathbf{r}, \hat{\mathbf{s}}, t)$ is a consequence of the medium's scattering properties.

The reduced component of the radiance can be found by solving [44]

$$\frac{\eta^x}{c} \frac{\partial L_r^x(\mathbf{r}, \hat{\mathbf{s}}, t)}{\partial t} + \hat{\mathbf{s}} \cdot \nabla L_r^x(\mathbf{r}, \hat{\mathbf{s}}, t) = -[\mu_t^x(\mathbf{r}) + \mu_a^{x \rightarrow m}(\mathbf{r})] L_r^x(\mathbf{r}, \hat{\mathbf{s}}, t), \quad (4)$$

with the following corresponding boundary condition

$$L_r^x(\mathbf{r}, \hat{\mathbf{s}}, t) = B_r^x(\mathbf{r}, \hat{\mathbf{s}}) \delta(t), \quad \mathbf{r} \in \partial V, \quad \hat{\mathbf{s}} \cdot \hat{\mathbf{n}} < 0. \quad (5)$$

Equations (4) and (5) allow obtaining the distribution of the reduced component of the radiance inside the medium. For short light pulses from an infinitely narrow laser beam incident on ∂V in the direction $\hat{\mathbf{s}}_0$ (in TD experimental systems pulse widths are on the order of a few tens of picoseconds down to about 100 femtoseconds), the spatial dependence of $L_r^x(\mathbf{r}, \hat{\mathbf{s}}, t)$ is that of a line source [44,45] whose strength is exponentially damped according to $\exp[-(\mu_t^x + \mu_a^{x \rightarrow m})z]$, where z is the depth measured from the incident point. Also, the intensity varies in time by “switching on” each part of the line source in accordance to the light speed in the medium as a time-retarded source. The diffuse component of the radiance $L_d^x(\mathbf{r}, \hat{\mathbf{s}}, t)$ satisfies the following radiative transfer equation and boundary conditions

$$\left[\frac{\eta^x}{c} \frac{\partial}{\partial t} + \hat{\mathbf{s}} \cdot \nabla + \mu_t^x(\mathbf{r}) + \mu_a^{x \rightarrow m}(\mathbf{r}) \right] L_d^x(\mathbf{r}, \hat{\mathbf{s}}, t) = \mu_s^x(\mathbf{r}) \int_{4\pi} p^x(\mathbf{r}, \hat{\mathbf{s}}, \hat{\mathbf{s}}') L_d^x(\mathbf{r}, \hat{\mathbf{s}}', t) d\Omega' + Q^x(\mathbf{r}, t), \quad (6)$$

$$L_d^x(\mathbf{r}, \hat{\mathbf{s}}, t) = R_p^x(\hat{\mathbf{s}}' \cdot \hat{\mathbf{n}}) L_d^x(\mathbf{r}, \hat{\mathbf{s}}', t), \quad \mathbf{r} \in \partial V, \quad \hat{\mathbf{s}}' = \hat{\mathbf{s}}' - 2(\hat{\mathbf{s}}' \cdot \hat{\mathbf{n}}), \quad \hat{\mathbf{s}} \cdot \hat{\mathbf{n}} < 0, \quad (7)$$

where the isotropic source term $Q^x(\mathbf{r}, t)$ is related to the reduced component $L_r^x(\mathbf{r}, \hat{\mathbf{s}}, t)$ as follows

$$Q^x(\mathbf{r}, t) = \mu_s^x(\mathbf{r}) \int_{4\pi} p^x(\mathbf{r}, \hat{\mathbf{s}}, \hat{\mathbf{s}}') L_r^x(\mathbf{r}, \hat{\mathbf{s}}', t) d\Omega'. \quad (8)$$

The solution satisfying Eqs. (4) and (5) can be substituted into Eq. (8) to obtain an expression for the source term $Q^x(\mathbf{r}, t)$. To calculate $Q^x(\mathbf{r}, t)$, the Henyey-Greenstein phase function [16], generally adopted in biomedical optics, can be employed

$$p^x(\mathbf{r}, \hat{\mathbf{s}}, \hat{\mathbf{s}}') = \frac{1 - (g^x(\mathbf{r}))^2}{4\pi \left[1 + (g^x(\mathbf{r}))^2 - 2(g^x(\mathbf{r}))^2 (\hat{\mathbf{s}} \cdot \hat{\mathbf{s}}') \right]}, \quad (9)$$

where $g^x(\mathbf{r})$ (the anisotropy parameter) describes the degree of anisotropy of the scattering. The Henyey-Greenstein phase function acceptably reproduces the properties of strong forward scattering of most biological tissues, with values of g^x between 0.7 and 0.9 [47].

In TD experimental systems, measurements are related to the diffuse component (ballistic photons cannot be detected in practice for tissue thicknesses considered here, *i.e.* on the order of a few millimeters to a few centimeters). Hence, the diffuse component $L_d^x(\mathbf{r}, \hat{\mathbf{s}}, t)$ is usually substituted in Eq. (6) by the total radiance $L(\mathbf{r}, \hat{\mathbf{s}}, t)$. Besides, the external source distribution (most frequently an array of collimated laser beams) is substituted in Eq. (6) by a distribution of internal sources created by the scattering that the source photons undergo in the medium. It is widespread to model each such as an internal source by approximating it as an isotropic point source located at one scattering length ($1/\mu_s'$, with $\mu_s' = (1-g)\mu_s$) inside the medium [17]. However, more elaborated source models such as a line of isotropic point sources [45] with an exponentially decaying intensity are more physically realistic as discussed above, and, therefore, better describe the highly anisotropic radiative field near the point of incidence of the laser beam. It is also possible to arrive at this conclusion after an analysis of the source term given in Eq. (8) and the distribution of the reduced component of the radiance $L_r^x(\mathbf{r}, \hat{\mathbf{s}}, t)$ in the medium.

Solving Eqs. (4), (5), (6) and (7) allows calculating the reduced and the diffuse components of the radiance and, consequently, the total radiance distribution in the medium. Equation (6) does not have a general analytic solution, except for simple geometries. Its numerical implementation for complex geometries is often computationally expensive. Thus, instead of solving Eq. (6) directly, or even use the P_N approximation, we propose to employ the TD-p SP_N approach we recently developed [34]. With the TD-p SP_N , the RTE for the diffuse component of the radiance $L_d^x(\mathbf{r}, \hat{\mathbf{s}}, t)$ (Eq. (6)) is transformed into a system of parabolic simplified spherical harmonics equations [31]. The finite set of equations is expressed in terms of the Legendre even moments of $L_d^x(\mathbf{r}, \hat{\mathbf{s}}, t)$ up to the truncated order N of the Legendre expansion. This order N is selected to be odd since even moments can be expressed in terms of odd moments, even in the time-dependent case (see [34]), by neglecting the time derivatives of the odd moments in analogy with the diffusion approximation [16]. The boundary conditions Eq. (7) are transformed accordingly and are also expressed in terms of the Legendre even moments of $L_d^x(\mathbf{r}, \hat{\mathbf{s}}, t)$.

Applying the time-dependent SP_N method to Eqs. (6) and (7) results in coupled parabolic PDEs (the TD-p SP_N model for the excitation light transfer) and corresponding boundary conditions (see [18,34] for the details of the derivation; boundary conditions in the time-independent and time-dependent cases are the same)

$$\left[\mathbf{C}^x + \frac{\eta^x}{c} \frac{\partial}{\partial t} \mathbf{T} \right] \Phi^x(\mathbf{r}, t) + \mathbf{D}^x \Phi^x(\mathbf{r}, t) = \mathbf{Q}^x(\mathbf{r}, t), \quad (10)$$

$$\mathbf{A}^x \Phi^x(\mathbf{r}, t) + \mathbf{B}^x \frac{\partial}{\partial \mathbf{n}} \Phi^x(\mathbf{r}, t) = \mathbf{0}, \quad \mathbf{r} \in \partial V, \quad (11)$$

where $\Phi^x(\mathbf{r}, t) = [\varphi_k^x(\mathbf{r}, t)]^T$, $k = 1, 2, 3, \dots, l_N$, $l_N = (N+1)/2$ is the vector of the composite moments functions $\varphi_k^x(\mathbf{r}, t)$ of the diffuse component of the radiance $L_d^x(\mathbf{r}, \hat{\mathbf{s}}, t)$ and N is the order of the approximation. The vector $\Phi^x(\mathbf{r}, t)$ is related to the vector

$\Psi^x(\mathbf{r}, t) = [\psi_k^x(\mathbf{r}, t)]^T$, $k = 0, 2, 4, \dots$ of the even Legendre moments $\psi_k^x(\mathbf{r}, t)$ of the radiance via a transformation matrix \mathbf{T}

$$\Psi^x(\mathbf{r}, t) = \mathbf{T}\Phi^x(\mathbf{r}, t). \quad (12)$$

\mathbf{T} is a matrix of constant numbers with no dependence on the optical coefficients or whatsoever; \mathbf{A}^x , \mathbf{B}^x and \mathbf{C}^x are matrices whose elements depend on the values of the optical coefficients of the medium; \mathbf{D}^x is a diagonal matrix operator; $\mathbf{Q}^x(\mathbf{r}, t)$ is a vector accounting for the source term and $\partial/\partial \hat{\mathbf{n}}$ denotes the gradient along the outward pointing normal $\hat{\mathbf{n}}$ to the boundary ∂V .

The entries of each matrix, in the same order that they appear in Eqs. (10) and (11), will now be described, up to the order $N = 7$, which is the highest order studied in the literature [18]. \mathbf{C}^x is a square symmetric matrix with l_N rows whose upper diagonals are given by

$$\begin{aligned} \text{diag}_0(\mathbf{C}^x) &= [\mu_0^x, (4/9)\mu_0^x + (5/9)\mu_2^x, (64/225)\mu_0^x + (16/45)\mu_2^x + (9/25)\mu_4^x, \\ & (256/1225)\mu_0^x + (64/245)\mu_2^x + (324/1225)\mu_4^x + (13/49)\mu_6^x] \\ \text{diag}_1(\mathbf{C}^x) &= [-(2/3)\mu_0^x, -(16/45)\mu_0^x - (4/9)\mu_2^x, -(128/525)\mu_0^x - (32/105)\mu_2^x - (54/175)\mu_4^x], \\ \text{diag}_2(\mathbf{C}^x) &= [(8/15)\mu_0^x, (32/105)\mu_0^x + (8/21)\mu_2^x], \\ \text{diag}_3(\mathbf{C}^x) &= [-(16/35)\mu_0^x], \end{aligned} \quad (13)$$

where the expression $\text{diag}_k()$ lists the elements on the k^{th} diagonal; the main diagonal is indexed by 0 and upper diagonals by 1, 2, ... consecutively. In these expressions appear the j -th order transport coefficients given by $\mu_j^x(\mathbf{r}) = \mu_a^x(\mathbf{r}) + \mu_a^{x \rightarrow m}(\mathbf{r}) + \mu_s^x(\mathbf{r}) [1 - (g^x(\mathbf{r}))^j]$.

Matrix \mathbf{T} is an upper triangular square matrix, also with l_N rows. Its inverse \mathbf{T}^{-1} has a very simple form

$$\mathbf{T}^{-1} = \begin{bmatrix} 1 & 2 & 0 & 0 \\ 0 & 3 & 4 & 0 \\ 0 & 0 & 5 & 6 \\ 0 & 0 & 0 & 7 \end{bmatrix}. \quad (14)$$

The diagonal matrix operator \mathbf{D}^x has the following entries

$$(D^x)_{i,i} = -\nabla \left[\frac{1}{(4i-1)\mu_{2i-1}} \nabla \right], \quad i = 1 \dots l_N. \quad (15)$$

The column vector $\mathbf{Q}^x(\mathbf{r}, t)$ is given by

$$\mathbf{Q}^x(\mathbf{r}, t) = [Q^x(\mathbf{r}, t), -(2/3)Q^x(\mathbf{r}, t), (8/15)Q^x(\mathbf{r}, t), -(16/35)Q^x(\mathbf{r}, t)]^T, \quad (16)$$

where the upper index T denotes matrix transposition throughout.

We do not reproduce here the complete expressions for the boundary matrices \mathbf{A}^x and \mathbf{B}^x appearing in the boundary conditions as they can be found in Appendix A of [18] (re-expressed in matrix form in Appendix C of [34]). These matrices depend on the values of the

optical coefficients at the boundary and involve angular moments of the angle-dependent Fresnel coefficient $R_F^x(\hat{\mathbf{s}} \cdot \hat{\mathbf{n}})$.

The normal component of the exiting photon current density vector can be calculated using the values of $\Phi^x(\mathbf{r}, t)$ and the optical coefficients at the boundary

$$J_n^x = \left[\mathbf{j}_1^x - \mathbf{j}_2^x (\mathbf{B}^x)^{-1} \mathbf{A}^x \right] \left(\Phi^x(\mathbf{r}, t) \Big|_{\mathbf{r} \in \partial V} \right), \quad (17)$$

where the expressions for vectors \mathbf{j}_1^x and \mathbf{j}_2^x appear in Appendix A below.

Equations (10) and (11) are the TD-pSP_N equations for the excitation light transfer at λ^x . The solution of this system converges asymptotically to transport solutions, *i.e.* there is an optimal order N for each physical situation. Before going further, we should note that this model was validated by Monte Carlo simulations for diffusive and diffusion defying regimes in a previous work [34]. In the diffusion defying regime it outperformed the DE, and better described time-resolved data for early arriving photons. Thus, Eqs. (10) and (11) are more appropriate than the DE to model the excitation light transfer at λ^x . Next, we introduce spatial finite element and temporal finite difference schemes to numerically solve Eqs. (10) and (11).

3.1.2 Numerical implementation of the TD-pSP_N equations for excitation light transfer

The finite element method (FEM) is a very flexible technique for numerically solving PDEs involving arbitrary complex and inhomogeneous geometries, such as can be the case for biological tissues. The use of the FEM to solve the RTE and the DE has been successfully carried out before [48–53]. To apply the FEM to our model, the domain of interest V is partitioned into l non-overlapping elements $\tau_j, j = 1, \dots, l$ joined at d vertex nodes. Then, the solution $\Phi^x(\mathbf{r}, t)$ is approximated by a piecewise polynomial and continuous function

$$\Phi_h^x(\mathbf{r}, t) = \sum_{i=1}^d \Phi_i^x(t) u_i(\mathbf{r}), \quad u_i(\mathbf{r}) \in \Omega_h \text{ where } \Omega_h \text{ is a finite-dimensional subspace spanned by}$$

the basis functions $u_i(\mathbf{r}), i = 1 \dots d$. If we substitute $\Phi_h^x(\mathbf{r}, t)$ in Eq. (10) and apply the Galerkin method to the result we obtain a set of discretized equations in terms of the nodal values $\tilde{\Phi}^x(t) = \{\Phi_i^x(t)\}_{i=1 \dots d}$. The final equations can be expressed in matrix notation in the time domain as

$$\left[\tilde{\mathbf{K}}^x + \tilde{\mathbf{M}}^x + \tilde{\mathbf{P}}^x + \left(\frac{\eta}{c} \right) \tilde{\mathbf{T}} \frac{\partial}{\partial t} \right] \tilde{\Phi}^x(t) = \tilde{\mathbf{F}}^x(t). \quad (18)$$

The structure of the system matrices $\tilde{\mathbf{K}}^x, \tilde{\mathbf{M}}^x, \tilde{\mathbf{P}}^x, \tilde{\mathbf{T}}$ and the source vector $\tilde{\mathbf{F}}^x(t)$ appearing in Eq. (18) will now be explained. The square sparse matrix $\tilde{\mathbf{K}}^x$ is a block diagonal matrix (we refer to diagonal 0 in our notation) composed of elemental “stiffness” matrices $\{\tilde{\mathbf{K}}_k^x\}_{k=1 \dots l_N}$ whose entries are given by

$$\tilde{K}_k^x(i, j) = \int_V \frac{1}{(4k-1)\mu_{2k-1}^x} \nabla u_i(\mathbf{r}) \cdot \nabla u_j(\mathbf{r}) dV, \quad k = 1 \dots l_N, \quad i, j = 1 \dots d. \quad (19)$$

The square sparse matrices $\widetilde{\mathbf{M}}^x$, $\widetilde{\mathbf{\Pi}}^x$ and, $\widetilde{\mathbf{T}}$ are composed of $l_N \times l_N$ block matrices $\left\{ \widetilde{\mathbf{M}}_{k_1, k_2}^x \right\}_{k_1, k_2=1 \dots l_N}$, $\left\{ \widetilde{\mathbf{\Pi}}_{k_1, k_2}^x \right\}_{k_1, k_2=1 \dots l_N}$, $\left\{ \widetilde{\mathbf{T}}_{k_1, k_2} \right\}_{k_1, k_2=1 \dots l_N}$ whose entries are respectively given by

$$\widetilde{M}_{k_1, k_2}^x(i, j) = \int_V C^x(k_1, k_2) u_i(\mathbf{r}) u_j(\mathbf{r}) dV, \quad k_1, k_2 = 1 \dots l_N, \quad i, j = 1 \dots d, \quad (20)$$

$$\widetilde{\Pi}_{k_1, k_2}^x(i, j) = \int_{\partial V} \frac{\Theta^x(k_1, k_2)}{(4k_1 - 1) \mu_{2k_1 - 1}^x} u_i(\mathbf{r}) u_j(\mathbf{r}) d\sigma, \quad k_1, k_2 = 1 \dots l_N, \quad i, j = 1 \dots d, \quad (21)$$

$$\widetilde{T}_{k_1, k_2}(i, j) = \int_V T(k_1, k_2) u_i(\mathbf{r}) u_j(\mathbf{r}) dV, \quad k_1, k_2 = 1 \dots l_N, \quad i, j = 1 \dots d, \quad (22)$$

where $C^x(k_1, k_2)$ and $T(k_1, k_2)$ are the elements of the matrices \mathbf{C}^x and \mathbf{T} , respectively. The term $\Theta^x(k_1, k_2)$ represents the elements of the matrix $\Theta^x = (\mathbf{B}^x)^{-1} \mathbf{A}^x$ which originates from the boundary conditions - Eq. (11). Finally, the source vector $\widetilde{\mathbf{F}}^x(t)$ can be written as a concatenation of l_N "load vectors" $\left\{ \widetilde{\mathbf{F}}_k^x(t) \right\}_{k=1 \dots l_N}$ given by

$$\widetilde{F}_k^x(t) = \int_V Q^x(k) u_i(\mathbf{r}) dV, \quad k = 1 \dots l_N, \quad i = 1 \dots d, \quad (23)$$

where $Q^x(k)$ are the components of the column vector $\mathbf{Q}^x(\mathbf{r}, t)$.

For the time-dependence of the equations, we use the finite difference method (FDM). Making use of a control parameter $\rho \in [0, 1]$ that determines the difference scheme, the latter can be written as

$$\left[\rho \widetilde{\mathbf{K}}^x + \rho \widetilde{\mathbf{M}}^x + \rho \widetilde{\mathbf{\Pi}}^x + \frac{1}{\Delta t} \left(\frac{\eta^x}{c} \right) \widetilde{\mathbf{T}} \right] \widetilde{\Phi}^{x, (n+1)} + \left[(1 - \rho) \widetilde{\mathbf{K}}^x + (1 - \rho) \widetilde{\mathbf{M}}^x + (1 - \rho) \widetilde{\mathbf{\Pi}}^x - \frac{1}{\Delta t} \frac{\eta^x}{c} \widetilde{\mathbf{T}} \right] \widetilde{\Phi}^{x, (n+1)} = \rho \widetilde{\mathbf{F}}^{x, (n+1)} + (1 - \rho) \widetilde{\mathbf{F}}^{x, (n)}, \quad (24)$$

where $\widetilde{\Phi}^{x, (n)}$ represents the solution of Eq. (18) at time n and Δt is the time step. Then, the finite difference scheme can be selected through the value of ρ . For $\rho = 1$, we get the implicit scheme, and for $\rho = 1/2$ we obtain the Crank–Nicholson scheme. The solution of Eq. (24) involves the inversion of sparse matrices of large dimensions, especially in 3D problems. From the solution of Eq. (24), we can determine the excitation fluence rate profile in the medium V . Hence, the time-dependent excitation of the fluorophores and their response over time at a wavelength λ^m of the fluorescence emission spectrum can be calculated. Next, we describe the temporal interaction between the excitation field and the fluorescence response over time by way of a second RTE_{SD}.

3.2 Time-dependent fluorescence light transfer

To describe the propagation of the fluorescence light at λ^m in the medium, we propose the time-dependent RTE_{SD} and its corresponding boundary condition. This time, ray divergence effects are considered because of the fluorophore distribution that acts as secondary internal sources. The corresponding equations are then

$$\left[\frac{\eta^m}{c} \frac{\partial}{\partial t} + \hat{\mathbf{s}} \cdot \nabla + \mu_t^m(\mathbf{r}) + (\nabla \cdot \hat{\mathbf{s}}) \right] L^m(\mathbf{r}, \hat{\mathbf{s}}, t) = \mu_s^m(\mathbf{r}) \int_{4\pi} p(\mathbf{r}, \hat{\mathbf{s}}, \hat{\mathbf{s}}') L_d^m(\mathbf{r}, \hat{\mathbf{s}}', t) d\Omega' + Q^m(\mathbf{r}, t), \quad (25)$$

$$L^m(\mathbf{r}, \hat{\mathbf{s}}, t) = R_F^m(\hat{\mathbf{s}}' \cdot \hat{\mathbf{n}}) L^m(\mathbf{r}, \hat{\mathbf{s}}', t), \quad \mathbf{r} \in \partial V, \quad \hat{\mathbf{s}}' = \hat{\mathbf{s}}' - 2(\hat{\mathbf{s}} \cdot \hat{\mathbf{n}}), \quad \hat{\mathbf{s}} \cdot \hat{\mathbf{n}} < 0, \quad (26)$$

where the terms appearing in Eqs. (25) and (26) have the same meaning as in Eqs. (1) and (2), but considering the values of the optical properties at the emission wavelength λ^m . The term $\nabla \cdot \hat{\mathbf{s}}$ accounts for ray divergence effects [20] and its contribution becomes non-negligible near sources, especially for point-like sources. For an isotropic point source located in a medium with constant refractive index $\nabla \cdot \hat{\mathbf{s}} = 2/r$, where r is the distance from the source [20]. The term $Q^m(\mathbf{r}, t)$ denotes the source of fluorescence

$$Q^m(\mathbf{r}, t) = \frac{\zeta \mu_a^{x \rightarrow m}(\mathbf{r})}{\tau} \int_{t'=0}^{t'=t} \phi^x(\mathbf{r}, t') \exp\left(-\frac{t-t'}{\tau}\right) dt', \quad (27)$$

which expresses the temporal interaction, through the convolution operation, between the excitation field and the fluorescent emission. Here, ζ denotes the quantum yield of the fluorophore considered, and ϕ^x is the fluence rate of the excitation field. Finding the solution of Eqs. (25) and (26) poses similar problems as to finding the solution of Eqs. (5) and (6). Thus, we resort to the time-dependent SP_N method [34] to Eqs. (25) and (26) and follow the same steps as for the excitation field in order to find a numerical solution. This results in a system of coupled time-dependent parabolic SP_N equations (the TD-p SP_N model for the fluorescence light transfer) and corresponding boundary conditions, *i.e.*

$$\left[\mathbf{C}^m + \frac{\eta^m}{c} \frac{\partial}{\partial t} \mathbf{T} \right] \Phi^m(\mathbf{r}, t) + \mathbf{D}^x \Phi^m(\mathbf{r}, t) = \mathbf{Q}^m(\mathbf{r}, t), \quad (28)$$

$$\mathbf{A}^m \Phi^m(\mathbf{r}, t) + \mathbf{B}^m \frac{\partial}{\partial \mathbf{n}} \Phi^m(\mathbf{r}, t) = \mathbf{0}, \quad \mathbf{r} \in \partial V. \quad (29)$$

The source term $\mathbf{Q}^m(\mathbf{r}, t)$ is given by the same expression as that found in Eq. (16), but with $\mathbf{Q}^x(\mathbf{r}, t)$ replaced by $\mathbf{Q}^m(\mathbf{r}, t)$ given in Eq. (27). Each term in Eqs. (28) and (29) have the same meaning as in Eqs. (10) and (11), but considering the values of the optical coefficients at a fluorescence wavelength λ^m . Equations (28) and (29) are the TD-p SP_N equations for the fluorescence light transfer at λ^m . It models, as before for the excitation wavelength λ^x , the propagation of light coming from a source distribution in the tissue, presenting no conceptual difference from Eqs. (10) and (11) and the original model [34]. Thus, Eqs. (28) and (29) are more suitable than the DE to model fluorescence light transfer in presence of small geometries and inhomogeneities with high absorption coefficients, as vascularized tissues and fluorescent inclusions. Next, Eqs. (28) and (29) are solved numerically by introducing an FEM scheme to account for the spatial dependence and an FDM scheme for the temporal dependence. Similarly to the excitation field, we thereby obtain

$$\left[\rho \tilde{\mathbf{K}}^m + \rho \tilde{\mathbf{M}}^m + \rho \tilde{\mathbf{\Pi}}^m + \frac{1}{\Delta t} \left(\frac{\eta^m}{c} \right) \tilde{\mathbf{T}} \right] \tilde{\Phi}^{m,(n+1)} + \left[(1-\rho) \tilde{\mathbf{K}}^m + (1-\rho) \tilde{\mathbf{M}}^m + (1-\rho) \tilde{\mathbf{\Pi}}^m - \frac{1}{\Delta t} \frac{\eta^m}{c} \tilde{\mathbf{T}} \right] \tilde{\Phi}^{m,(n)} = \rho \tilde{\mathbf{F}}^{m,(n+1)} + (1-\rho) \tilde{\mathbf{F}}^{m,(n)}. \quad (30)$$

The terms appearing in Eq. (30) have a similar interpretation as those in Eq. (24). With this numerical scheme, one can then obtain the fluorescence light transfer in a volume of biological tissue considering all of its complexity in terms of geometry and heterogeneity.

4. Excitation and fluorescence light propagation in a homogeneous medium with a fluorescent inclusion

In this section, we perform numerical experiments in which we compute the time-dependent transfer of excitation and fluorescence light in tissue-like media for two cases of practical interest: (1) a homogeneous cylinder with an embedded fluorescent inclusion which is often used in validation experiments, and (2) a rodent-shaped homogeneous body with an organ filled with a fluorescent agent which is of interest in small animal molecular imaging. The numerical experiments concerning the cylinder involve three types of fluorescent inclusions: (i) point-like, (ii) spherical with sharp boundary, and (iii) spherically symmetric with radially Gaussian distributed absorption. The inclusions are centered at the same position to compare the effect of their spatial distribution. In the numerical experiments, we employ the numerical schemes of Eqs. (24) and (30) with $\rho = 1$ (FDM implicit scheme) to determine the excitation and the fluorescent fluence rate profiles in the media.

4.1 Homogeneous small cylinder with fluorescent inclusion

The cylinder is a simple geometry that is very common in biomedical optics laboratories such as for validating tomographic reconstruction algorithms. A small homogeneous cylinder containing a tissue-like medium mimics a small volume of biological tissue. In our experiment we use a cylinder of 3 cm height and 1.5 cm radius filled with a thick homogeneous medium. The following values for the optical properties of the medium are used: refractive index $\eta = 1.4$, absorption coefficient $\mu_a = 0.13 \text{ cm}^{-1}$, scattering coefficient $\mu_s = 100 \text{ cm}^{-1}$ and anisotropy parameter $g = 0.9$. Such optical properties can be experimentally obtained in samples with a mixture of IntralipidTM solution (concentration around 1%), and ink (as an example, see [51] for details on the experimental procedure). Since the Henyey-Greenstein phase function (9) is used in the numerical experiments, herein we always assume $g = 0.9$ [47].

In our first experiment, a fluorescent point inclusion is placed inside the cylinder at Cartesian coordinates $x = 0.7 \text{ cm}$, $y = 0.7 \text{ cm}$ and $z = 1.5 \text{ cm}$, see Fig. 2 (letter **I** denotes the position of the inclusion).

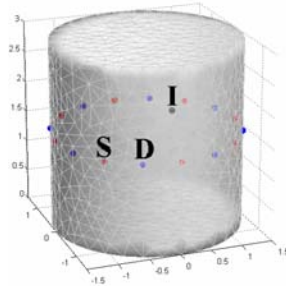


Fig. 2. Mesh of the cylinder.

The inclusion has the fluorescence properties of indocyanine green (ICG, NIR fluorophore with absorption/emission peaks at 780nm/830nm) with a quantum yield $\zeta = 0.012$, absorption coefficient $\mu_a^{x \rightarrow m} = 3 \text{ cm}^{-1}$ and fluorescence lifetime $\tau = 0.56 \text{ ns}$. Such optical properties of the fluorescence inclusion can be experimentally obtained using an aqueous solution of ICG at a concentration of around $10 \mu\text{mol/L}$ (see for example the experimental procedure in [24,25], see also [54] for the link between $\mu_a^{x \rightarrow m}$ and the concentration through the molar extinction

coefficient; such values are typical in small animal imaging [10]). The scattering coefficient and anisotropy parameter within the inclusion are assumed the same as for the surrounding medium. As external sources of excitation, 8 infinitely narrow and collimated laser beams are placed in a plane perpendicular to the axis of the cylinder at half the height of the cylinder (hereon, we refer to this plane as the source plane, where the point inclusion is also located). Here, sources are interlaced by a group of 8 detectors. The position of one of the sources and one of the detectors are denoted by letters **S** and **D**, respectively in Fig. 2. The sources emit individual pulses (a pulse which can be described analytically as a Dirac delta function in time) and they are turned on simultaneously in this experiment. For this physical situation, the TD- pSP_N equations with $N = 3$ for both the excitation and the fluorescence light transfer (Eqs. (10), (11), (28) and (29)) are solved using the FEM-FDM scheme discussed above with $\rho = 1$ (see Eqs. (24) and (30)). The order $N = 3$ is selected as it was shown to provide good results in previous work dealing with similar physical situations [18,34]. This choice also fits our goal of reducing computation time. For the purpose of the FEM, the medium is divided into tetrahedral elements (5969 nodes and 29219 elements) using a non-regular Delaunay triangulation. The mesh is refined in the region of the inclusion for a better analysis and the injection of the laser beam in the medium is modeled as an internal line source (see [53,55,56] for the topic of source term modeling and implementation using the FEM). The excitation and fluorescence fluence rate spatial profiles in the source plane for times of 0.15, 0.3 and 1.50 ns are shown in Fig. 3. These times are selected considering the temporal variation of the fluorescence fluence in the source plane, near and after the maximum of the fluence values in that plane. Figure 3 displays the effect on the excitation field of the higher absorption at the point inclusion (upper row) along with the variation in time of the fluorescence field due to the fluorescent point inclusion (lower row).

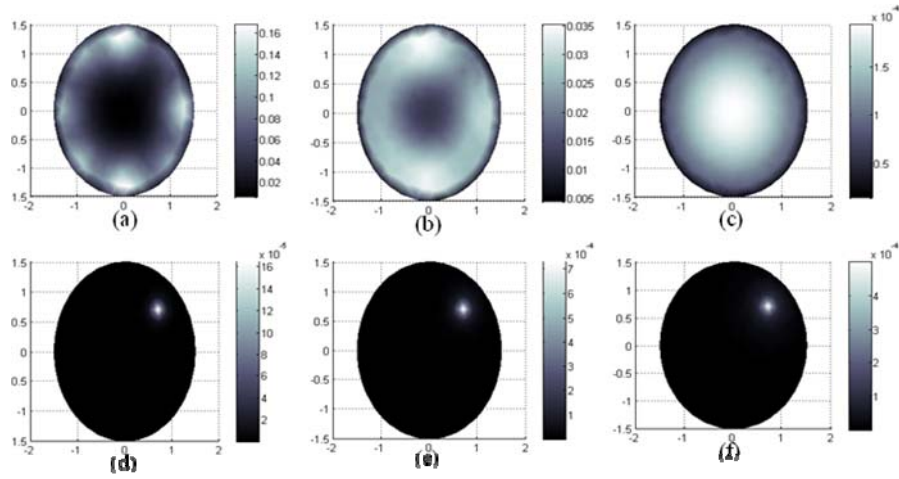


Fig. 3. Excitation and fluorescence fluence spatial distributions for a fluorescent point inclusion (upper and lower rows) in the source plane for 0.15, 0.3 and 1.5 ns (left to right).

In the second numerical experiment we change the fluorescent point inclusion for a fluorescent spherical inclusion with sharp edges, see Fig. 4. This time we study a non-point fluorescent inclusion since real inclusions are generally not point-like. The geometrical and optical properties of the cylinder are the same as in the previous numerical experiment, including the source distribution.

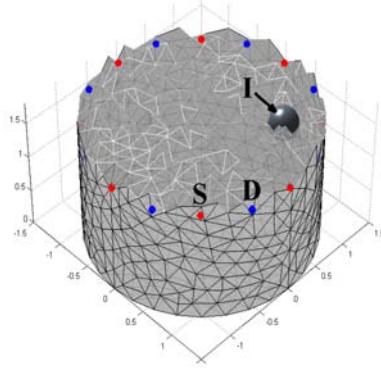


Fig. 4. Mesh of the cylinder cut at half of its height. The spherical absorbing inclusion is shown in grey.

The radius of the fluorescent spherical inclusion is 0.2 cm, which represents a volume of fluorescence similar to those used in experiments made in our laboratory [24,25]. Its center is located at Cartesian coordinates $x = 0.7$ cm, $y = 0.7$ cm and $z = 1.5$ cm. As above, we solve the TD-p SP_N equations with $N = 3$ for the excitation and the fluorescent light transfer using the FEM-FDM scheme with $\rho = 1$. Figure 5 shows the excitation and fluorescence fluence rate temporal profiles in the source plane for times of 0.15, 0.3 and 1.50 ns.

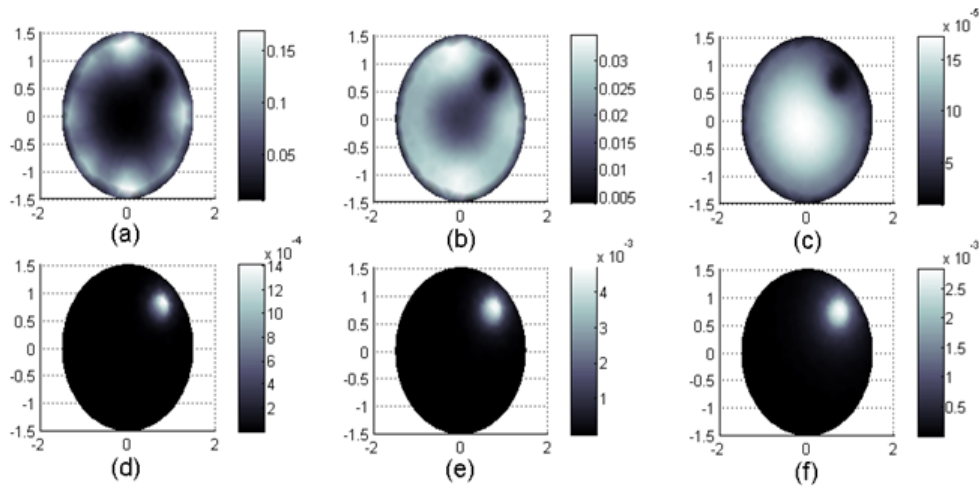


Fig. 5. The excitation and the fluorescent fluence profiles for a fluorescent spherical inclusion (upper and lower rows) at the source plane for 0.15, 0.3 and 1.5 ns (left to right).

Times are selected as before, near and after the maximum of the fluorescence fluence values. The excitation field images (upper row) clearly display a rounded darkening where the fluorescent inclusion is located. Simultaneously (see lower row in Fig. 5), the spatial extent of the zone where there is a fluorescence response increases, as well as the fluorescence fluence values since more of the inclusion is excited - also compare the fluence values in Fig. 5(e) with those in Fig. 3(e). Thus, due to the larger zone of the inclusion, fluorescence measurements at the boundary will reach higher values in the extended inclusion case compared to that of the point inclusion case. Next, we increase the complexity of our physical situation by placing in the previously described homogeneous cylinder a distributed inclusion *i.e.* a non-point inclusion with non-sharp edges. This physical situation represents a case where the distribution of the fluorescent substance fades out, as could be the case for instance of ICG extravasation in tumors [57]. To represent such a physical situation in a simplified

manner, we consider a spherically symmetric fluorescent inclusion having a radially distributed absorption that decays with a Gaussian dependence. The inclusion is centered at Cartesian coordinates $x = 0.7$ cm, $y = 0.7$ cm and $z = 1.5$ cm (as in the previous cases) and with $\mu_a = 3$ cm⁻¹ at the center (peak value) and standard deviation $\sigma = 0.2$ cm. The excitation and fluorescence light transfer are calculated by the described numerical FEM-FDM scheme (with $\rho = 1$) for the TD-pSP_N equations with $N = 3$. Figure 6 shows the excitation and fluorescence fluence rate temporal profiles in the source plane for times 0.15, 0.3 and 1.50 ns (chosen as before). As can be seen, there is a difference with the previous cases in the excitation field (upper row) and the fluorescence response (lower row) because of the spreading of the values of the absorption coefficient of the fluorescent inclusion. To further analyze the effects of considering non-point fluorescent inclusions, fluorescence time-domain data (fluence values) are obtained at a group of 8 detector positions located in the source plane (see Fig. 2 or Fig. 4 where the position of one of the detector positions is labeled as **D**).

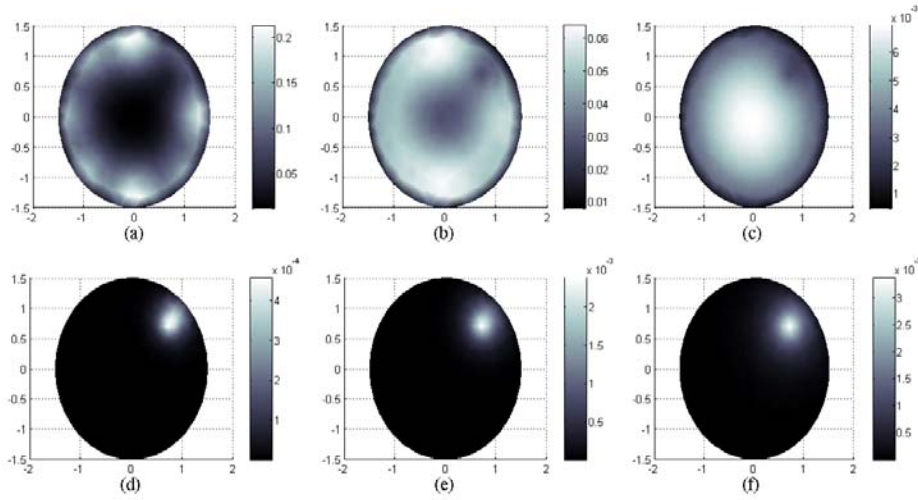


Fig. 6. The excitation and the fluorescent fluence profiles for a fluorescent distributed inclusion (upper and lower rows) at the source plane for 0.15, 0.3 and 1.5 ns (left to right).

We plot in Fig. 7 the data at the nearest detector to the inclusion's center (purposely chosen to be the same for all three types of fluorescent inclusion for comparison purposes - Cartesian coordinates $x = 0.7$ cm, $y = 0.7$ cm and $z = 1.5$ cm). As can be seen, the amplitude of the fluorescence response increases with the size of the fluorescent inclusion.

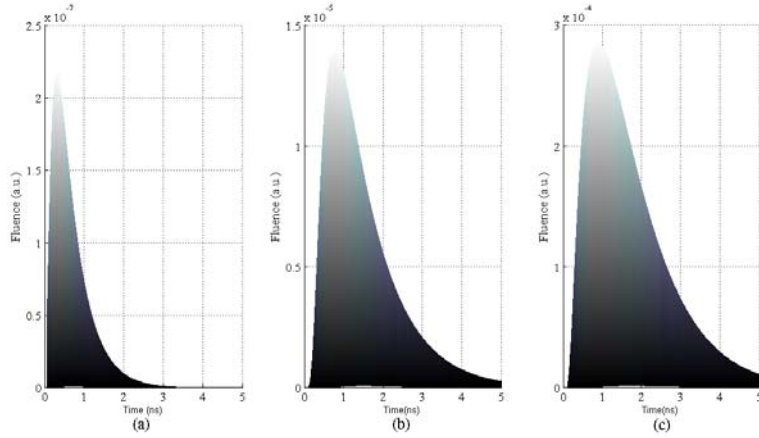


Fig. 7. Fluorescent measurement temporal profiles at the nearest detector to the center of the fluorescent inclusions; (a) point inclusion, (b) spherical inclusion, (c) Gaussian distributed inclusion.

More importantly, there is a noteworthy change in the shape of the curve. Going from the point inclusion (Fig. 7(a)) to the distributed inclusion (Fig. 7(c)), there are some significant changes: the rising edge is less abrupt, the peak of the curve is shifted in time and the tail is longer. It means that neglecting the spatial dimensions of fluorescent inclusions should be done carefully, especially in source reconstruction algorithms that use specific features of the time curve. For example, a shift in the peak of the distribution could occur because of a change in the position of the inclusion as discussed in [58], but it could also be due to a change in the spatial extent of the inclusion. Fluorescence wavefronts from several detectors, similarly as we calculated before, have been used to compute early photon arrival time surfaces (EPATs), which are currently exploited in the development of early arrival time reconstruction algorithms for point-like fluorescent inclusions [24,25].

4.2 Rodent-shaped homogenous body with fluorophore-filled organ

Our next numerical experiment makes use of a realistic 3D shape geometry consisting of the torso part of a rodent shape (rat or mouse), which is assumed to be homogenous, see Fig. 8.

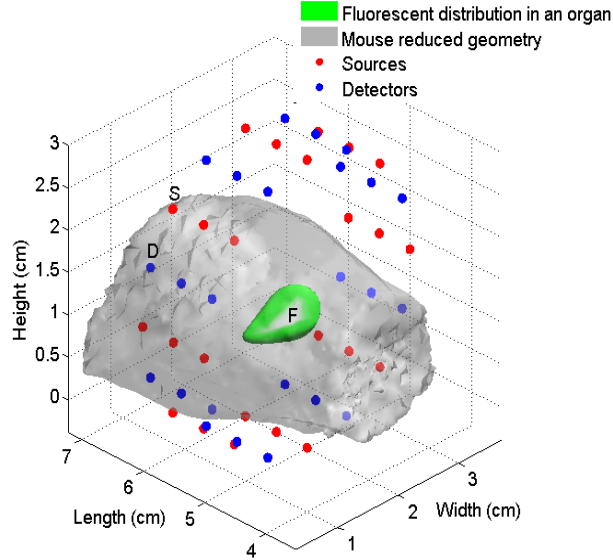


Fig. 8. Representation of the torso of the small animal.

This shape has been adapted from the Digimouse model [59]. Rats and mice account for up to 95% of animal models used in biomedical research, becoming a geometry of high interest in diffuse optical tomography of small animals [1–4]. For the present purposes, the optical properties within the volume are assumed to be the same as for the homogeneous cylinder considered in the previous section. A fluorescent inclusion mimicking an organ filled with a fluorophore having the properties of ICG is placed inside the homogeneous volume (see Fig. 8). The optical properties of the fluorescent inclusion are the same as for the inclusions embedded in the cylinder of the previous section. Twenty-four (24) excitation sources in the form of infinitely narrow and collimated laser beams and grouped in three different parallel planes (8 in each plane) are positioned around the object as shown in Fig. 8. The sources emit individual pulses (Dirac delta functions in time), and are turned on simultaneously in the experiment. To numerically solve the TD- pSP_3 model given in Eqs. (10), (11), (28) and (29) for the excitation and fluorescence light transfer ($N = 3$ is chosen for the same reasons as above), a fine mesh of 58244 nodes and 198089 elements was used. The mesh is refined in the zone where the organ is located to gain in resolution in that region. The laser beams are projected onto the mesh to determine the exact locations where excitation light is injected. As before, the injection of the laser beams in the medium is modeled as internal line sources. Here, a 3D model of the outer surface of the animal is obtained from the Digimouse mesh, but in a real small animal imaging session, the 3D outer surface of the animal can be measured optically by a number of 3D computer vision (CV) techniques involving structured illumination of the object to be imaged, such as spot ranging, light striping (or laser profilometry), or projected encoded patterns [60] as exemplified in [61,62]. The 3D data obtained via such 3D CV techniques allow obtaining a surface mesh model of the object, from which a volume mesh (as that in Fig. 8) can be built.

Figure 9 shows the excitation and fluorescence fluence rate profiles in a plane parallel to the xy plane at a height of 1 cm (along the vertical axis in Fig. 8) for times of 0.3, 0.6 and 1 ns (left to right). Times are selected following the same criterion as in the numerical experiments for the cylinder, by analyzing the time profile of the fluorescent response in that plane (Fig. 9, lower row). Even if the analysis of the images is more complicated in the case of the small animal torso due to the non-symmetrical position of the sources related to the inclusion, the effect of the inclusion's high absorption on the excitation field (upper row in Fig. 9) and the

time variation of the fluorescence (lower row in Fig. 9) can clearly be seen. As in the numerical experiments with the cylindrical geometry, different kinds of physical situations can eventually be studied.

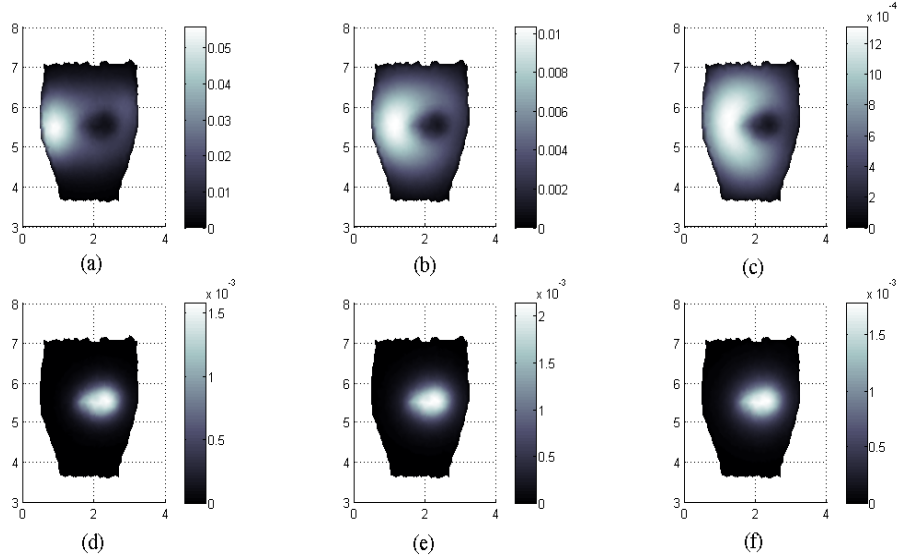


Fig. 9. Excitation and fluorescence fluence profiles (upper and lower rows respectively) in a plane at a height of 1 cm (see Fig. 6) for 0.3, 0.6 and 1.0 ns (left to right).

5. Conclusions

In this paper we developed a theoretical and numerical framework for modeling light propagation at both the excitation and fluorescence wavelengths by employing the TD- pSP_N model. This model comprehends two sets of coupled parabolic PDEs, with associated boundary conditions with matrix coefficients, for describing the time evolution of the excitation and fluorescence light fields, along with the coupling of the two fields through the fluorescence dynamics that involve the lifetime of the fluorophore considered. We introduced an FEM (finite element method) approach for the spatial dependence combined with an FDM (finite difference method) scheme for the temporal dependence of the fields. The exposed FEM-FDM method allows calculating the time-dependent profile of the excitation and of the fluorescence fluence rates for inhomogeneous media with arbitrary geometries, such as biological media.

Numerical experiments employing the FEM-FDM methodology were performed for two different geometries and allowed modeling the fluorescence response in the time domain. For both cases, results for the order $N = 3$ of the SP_N approximation were provided. When exploring higher orders in our model, we found that there was not a significant change in the results. Therefore, $N = 3$ is the optimal order for the physical situations we considered. The first geometry was a cylinder resembling a small volume of biological tissue incorporating a fluorescent inclusion. Such geometry is often encountered for validating diffuse optical tomography reconstruction algorithms. We examined three types of fluorescent inclusions: point-like, spherical with sharp boundary, and spherically symmetric with radially decaying Gaussian distributed absorption. We analyzed the effect of having non-point inclusions in our calculations. Our results clearly show the changes in the temporal profile of the fluorescence response owing to the spatial extent of the fluorescence distribution. To our knowledge, this is the first time this is reported. We thus arrive at the important conclusion that neglecting the dimensions of non-point fluorescent distributions in tissues is a possible source of errors in

fluorescent source reconstructions algorithms that use specific features of the time-dependent fluorescence curve.

The second geometry was a realistic torso shape of a rat or mouse, with a fluorescent inclusion having the closed shape of an organ. In this case, the geometry and the excitation source distribution feature increased complexity. Additionally, the excitation beams have been projected on the FEM surface to reproduce real conditions of non-contact small animal DOT and FDOT experiments. In both geometries the effects of the increased absorption coefficient due to the fluorescent inclusion was observed in the evolution of the excitation field at different times. Moreover, the fluorescence decay with time was reproduced. Taking into account the present, as well as former results [18,34], it may be concluded that the model is able to describe excitation and fluorescent light transfer in small geometries with high absorption coefficients and in nondiffusive domains as may be found in small animal DOT and FDOT imaging. An additional attribute of the model developed is the fact that it incorporates modern features to describe light propagation in biological tissues near sources by accounting for ray divergence. The proposed model shows substantial potential for serving as a forward model in FDOT reconstruction methods for optical imaging of biological tissues using either whole measured time-dependent curves or early photon time-of-flight methods. Finally, this work will eventually allow studying the dynamics of fluorescence in biological tissues via the fluorescence lifetime and its dependence on local biochemical environmental parameters.

Appendix

Vectors \mathbf{j}_1^i and \mathbf{j}_2^i at the wavelength λ^i have the following expressions

$$\begin{aligned} \mathbf{j}_1^i = & [1/4 + J_0, (1/4 + J_0)(-2/3) + (5/16 + J_2)(1/3), \\ & (1/4 + J_0)(8/15) + (5/16 + J_2)(-4/15) + (-3/32 + J_4)(1/5), \\ & (1/4 + J_0)(-15/35) + (5/16 + J_2)(8/35) + (-3/32 + J_4)(-6/35) + (13/256 + J_6)(1/7)], \end{aligned} \quad (\text{A1})$$

$$\mathbf{j}_2^i = \left[-\left(\frac{0.5 + J_1}{3\mu_{a1}^i} \right), \left(-\frac{J_3}{7\mu_{a3}^i} \right), \left(-\frac{J_5}{11\mu_{a5}^i} \right), \left(-\frac{J_7}{15\mu_{a7}^i} \right) \right], \quad (\text{A2})$$

where the coefficients J_1, J_2, \dots, J_7 can be found in Appendix A of [18].

Acknowledgments

J. Bouza-Domínguez acknowledges financial support from the FQRNT. Y. Bérubé-Lauzière acknowledges financial support from an NSERC Discovery Grant (Canada) for the present work. Yves Bérubé-Lauzière is member of the FRSQ-funded Centre de recherche clinique Étienne-Le Bel.